Magma flux at Okmok Volcano, Alaska, from a joint inversion of continuous GPS, campaign GPS, and interferometric synthetic aperture radar

Juliet Biggs,[1,2] Zhong Lu,[3] Tom Fournier,[4,5] and Jeffrey T. Freymueller[6]

Received 22 March 2010; revised 25 August 2010; accepted 31 August 2010; published 1 December 2010.

[1] Volcano deformation is usually measured using satellite geodetic techniques including interferometric synthetic aperture radar (InSAR), campaign GPS, and continuous GPS. Differences in the spatial and temporal sampling of each system mean that most appropriate inversion scheme to determine the source parameters from each data set is different. Most studies either compare results from independent inversions or subsample the data sets to the lowest common factor. It is unclear whether differences in the solution reflect differences in source behavior, differences in measurement bias, or differences in inversion technique. Here we develop a single inversion procedure that captures the benefits of each system, especially the daily sampling of continuous GPS and the high spatial resolution of InSAR. Okmok Volcano, Alaska, is an ideal target for such a test because a long series (<15 years) of InSAR and continuous GPS measurement exists and the source is almost continuously active and in a stable location.

Citation: Biggs, J., Z. Lu, T. Fournier, and J. T. Freymueller (2010), Magma flux at Okmok Volcano, Alaska, from a joint inversion of continuous GPS, campaign GPS, and interferometric synthetic aperture radar, *J. Geophys. Res.*, *115*, B12401, doi:10.1029/2010JB007577.

1. Introduction

1.1. Challenges of Joint Inversion

[2] Both GPS and interferometric synthetic aperture radar (InSAR) are satellite-based methods for measuring surface displacements on the scale of millimeters to centimeters. By using simple geometric models of the magma chamber, it is possible to convert surface displacements into a volume flux [*Mogi*, 1958; *Okada*, 1985; *Fialko et al.*, 2001a] and it would appear to be a simple task to combine GPS and InSAR observations to provide a record of the magma flux with time. However, the spatial and temporal sampling of the records are sufficiently different to complicate the task.

[3] GPS measures the full three-dimensional surface displacement field at instruments located on the ground. GPS measurements are either made in campaign mode (receivers are used to measure the positions of an array of fixed markers at repeated intervals, typically years apart) and continuous (the receiver is fixed in position and provides daily measurements). InSAR records the projection of the displacement field into a single line-of-sight vector at dense grid of measurement points. By combining InSAR images from different angles, the full 3-D component can be calculated [*Wright et al.*, 2004; *Fialko et al.*, 2001b], alternatively, if a sufficiently dense grid of three-component GPS measurements are available, the InSAR and GPS can be combined to produce a three-dimensional map of displacements [e.g., *Gudmundsson et al.*, 2002; *Samsonov and Tiampo*, 2006]. The satellites repeat their tracks typically every 24–46 days (depending on the orbit), but not all combinations of images can be used due to baseline restrictions [*Bürgmann et al.*, 2000].

[4] Time series methods for determining the evolution of surface displacements on a point by point basis are well established (e.g., SBAS [*Berardino et al.*, 2002], permanent scatterers [*Ferretti et al.*, 2001]) and modeling techniques exist to combine observations from a single time step at different locations [*Mogi*, 1958; *Okada*, 1985; *Fialko et al.*, 2001a]. Most authors either concentrate on a single measurement type [*Lu et al.*, 2005; *Fournier et al.*, 2009], jointly invert the cumulative displacement fields [*Biggs et al.*, 2009; *Cervelli et al.*, 2002] or compare volume estimates derived separately.

[5] We adapt the method of *Berardino et al.* [2002] to combine campaign GPS, continuous GPS and InSAR observations to provide a single time series of volume flux which benefits from the spatial and temporal advantages of both techniques. We chose to test the joint inversion on data from Okmok Volcano, Alaska because of the almost continuous

[1]Rosenstiel School of Marine and Atmospheric Science, University of Miami, Miami, Florida, USA.
[2]Now at NCEO, Department of Earth Sciences, University of Oxford, Oxford, UK.
[3]USGS Cascades Volcano Observatory, Vancouver, Washington, USA.
[4]Department of Earth and Atmospheric Sciences, Cornell University, Ithaca, New York, USA.
[5]Now at Department of Earth Science, Rice University, Houston, Texas, USA.
[6]Geophysical Institute, University of Alaska Fairbanks, Fairbanks, Alaska, USA.

0148-0227/10/2010JB007577

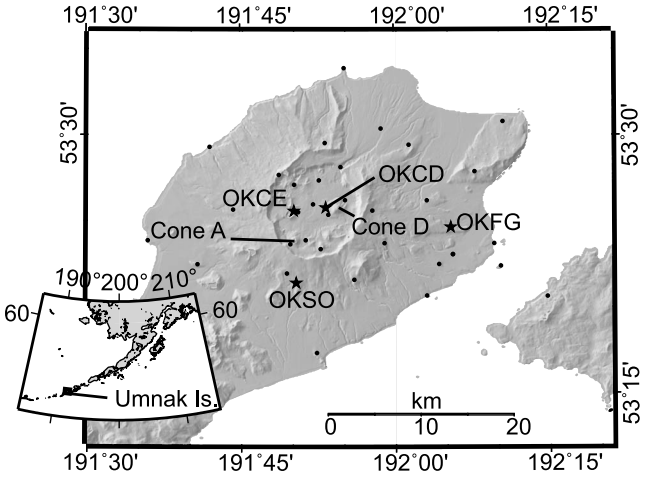

Figure 1. Topographic map of Okmok Volcano showing location of GPS sites and eruptive features. Stars are continuous GPS sites OKCD, OKCE, OKCF, OKSO. Small circles are campaign GPS sites.

geodetic activity, simplicity and stability of the magma source and large archive of geodetic data.

1.2. Okmok Volcano

[6] Okmok is a shield volcano located on Umnak Island in the Aleutian Chain. Okmok has had an eruption every 10–20 years for the past 200 years [*Miller et al.*, 1998] including most recently eruptions in 1997 and 2008. The 10 km diameter summit caldera was formed by eruptions 12,000 and 2500 years ago [*Finney et al.*, 2008] and contains a number of features related to subsequent eruptions (Figure 1). The 1997 eruption emanated from Cone A and produced a basaltic lava flow 5 km long and tens of meters thick [*Lu et al.*, 2003]; the 2008 eruption produced new vents located near Cone D and produced mainly tephra, a result of magma interaction with the water table [*Larsen et al.*, 2009].

1.3. Data Availability

[7] Geodetic observations have been used to measure surface deformation at Okmok volcano since 1992 and show inflation prior to the 1997 eruption, coeruptive deflation and the continued inflation [*Lu et al.*, 2000, 2005; *Mann et al.*, 2002]. The geodetic data used in this paper have already been published by *Lu et al.* [2005, 2010] and *Fournier et al.* [2009], and we provide a brief summary of the collection, processing, and resulting characteristics of each data set.

[8] There is a large archive of InSAR data available for Okmok from a range of satellites. Images are available from the European Space Agency Satellites ERS1, ERS2 and Envisat satellites, the Canadian Space Agency Satellite Radarsat 1 and the Japanese Satellite JERS. In this study we use 56 ERS1/2 interferograms, 35 Envisat interferograms, and 4 Radarsat interferograms (Table 1). Details of processing techniques and parameters are given by *Lu et al.* [2005, 2010].

[9] The first annual GPS campaigns began in 2000 with 19 sites and the network has gradually expanded to 33 sites. Installation of continuous GPS sites began in 2002 with OKCD, OKCE and OKCF; OKSO was added in 2004. Despite early problems with the permanent sites, reliable continuous data is available from 2003 onward. We use the GPS solution

Table 1. Interferograms Used in This Study From ESA's ERS1 and ERS2 Satellites, Envisat, and the Canadian Space Agency Satellite Radarsat-1[a]

Date 1	Date 2	Track
	ERS1/2	
19921031	19931120	115
19930529	19930703	115
19930719	19930823	344
19930804	19960927	072
19930908	19951006	072
19930911	19951009	115
19931013	19951006	072
19931013	19960927	072
19931016	19951009	115
19931101	19951025	344
19931101	19951026	344
19950607	19951129	344
19950901	19960927	072
19951006	19951216	072
19960203	19961026	072
19970508	19970717	344
19970508	19970925	344
19970701	19980825	115
19970701	19990706	115
19970701	20000725	115
19970717	19980910	344
19970717	19990617	344
19970717	20000914	344
19970909	19980929	115
19970909	20000829	115
19970925	19980910	344
19970925	19990617	344
19970925	20000914	344
19980825	20001003	115
19980910	19990930	344
19980910	20000914	344
19980910	20020815	344
19980929	19990601	115
19980929	20000829	115
19980929	20001107	115
19980929	20010710	115
19980929	20021008	115
19981031	20010915	072
19990617	20000706	344
19990617	20000914	344
19990706	20000725	115
19990807	20010915	072
19990903	20000818	451
19990914	20000725	115
19990930	20020815	344
19990930	20020919	344
20000706	20000914	344
20000818	20020719	451
20000826	20010915	072
20000826	20021005	072
20001107	20010710	115
20020625	20021112	115
20020630	20020908	179
20020815	20020919	344
20031009	20060824	344
20060530	20061017	115
	Envisat	
20010710	20021008	115
20030715	20040629	115
20030731	20040819	344
20030731	20050908	344
20030731	20051013	344
20030819	20050927	115
20030923	20041012	115
20031028	20040629	115
20040525	20041012	115
20040525	20050614	115

Table 1. (continued)

Date 1	Date 2	Track
20040819	20051013	344
20040819	20060615	344
20040827	20060901	451
20040907	20050719	115
20040907	20060808	115
20041001	20060728	451
20041012	20050614	115
20041020	20060712	222
20050526	20051013	344
20050622	20071010	222
20050630	20060824	344
20050630	20070913	344
20050719	20051101	115
20050719	20060704	115
20050719	20060808	115
20050719	20060912	115
20050812	20070921	451
20050927	20071002	115
20051013	20060615	344
20060615	20070705	344
20060720	20070913	344
20060816	20070801	222
20060816	20071010	222
20060901	20070921	451
20070801	20071010	222
	Radarsat	
20000824	20010702	900
20000917	20010819	900
20000917	20010912	900
20000927	20010829	800

[a]Dates are in year month day.

from *Fournier et al.* [2009], and readers are referred to that paper for further details on processing and sites. Following the approach of *Fournier et al.* [2009], we use all GPS sites to estimate a regional velocity during the inversion rather than using a reference station to remove common mode errors.

[10] All the studies by *Miyagi et al.* [2004], *Fournier et al.* [2009], *Lu et al.* [1998, 2000, 2005], *Mann et al.* [2002], and *Masterlark* [2007] find a satisfactory fit using a point source within a homogenous isotropic elastic half-space [*Mogi*, 1958]. *Lu et al.* [2010] investigate more complex source geometries and find that a prolate spheroid also provides a satisfactory fit to the data but fails the F test. *Masterlark* [2007] shows that while the assumptions of a homogeneous, isotropic, Poisson-solid half-space provide a good fit to the data, the errors associated with these assumptions can greatly exceed observation uncertainties and more complex rheological structures provide a more physically sensible solution.

2. Method

[11] The short baseline subset approach (SBAS) of *Berardino et al.* [2002] produces a time series of displacements from sets of interconnected interferograms. In this section we provide a simplified description of the SBAS algorithm and then extend it (1) to include continuous and campaign GPS data and (2) to combine different components and/or look vectors using a source model. Each GPS time series is treated as an independent SBAS subset in the inversion method.

2.1. Cumulative Displacement From InSAR

[12] An individual interferogram, i_{ij}, records the incremental ground deformation between two acquisition dates, t_i and t_j. For a set of acquisitions in which it is possible to construct an interferogram between each pair of neighboring acquisitions, simply starting with the first interferogram and adding on subsequent interferograms will produce a time series of the total displacement between the starting time and each acquisition date, d_i. Due to the constraints of baseline, Doppler and coherence, such a scenario is unlikely to exist outside of synthetic data sets. However, provided there are at least as many linearly independent interferograms as acquisitions and that the chain of interferograms is not broken at any point, it is possible to do a least squares inversion to obtain the time series of displacement.

[13] The phase of an individual interferogram is obtained by essentially differencing the phase of two radar images, and is traditionally represented by

$$\phi_{mn} = \frac{4\pi}{\lambda}(c_m - c_n) + \epsilon \tag{1}$$

where ϕ_{mn} is the phase of the interferogram, λ is the satellite wavelength, and c_m and c_n are the line-of-sight (LOS) displacements at time m and time n, respectively. For clarity of explanation at this stage, we assume that the contributions from orbital, atmosphere, baseline and choice of reference pixel are negligible; a reasonable assumption given the magnitude of the volcanic signals we will consider.

[14] The usual method of converting these observations into cumulative LOS displacements is to define a system of linear equations. Let $x_c = [c_A, c_B, c_C \ldots]$ be the vector of cumulative LOS displacement values to be found where c_B is the total LOS displacement which has occurred by the acquisition at time B. Let $b = [i_{AB}, i_{BC}, i_{BD} \ldots]$ be the vector containing the known incremental range changes from the interferograms. These values can be linked by the matrix equation, $\mathbf{A_c x_c} = \mathbf{b}$ where $\mathbf{A_c}$ is the design matrix.

[15] We consider a system of N interferograms constructed from S acquisitions. To determine the components of $\mathbf{A_c}$ we define the $1 \times S$ matrix $\mathbf{L}$ which contains the acquisition dates in chronological order and the $2 \times N$ matrix $\mathbf{H}$ whose rows represent the start and end dates of each interferogram. Then, $\mathbf{A_c}_{ij} = -1$ for $\mathbf{H_{i1}} = \mathbf{L_j}$ and $\mathbf{A_c}_{ij} = 1$ for $\mathbf{H_{i2}} = \mathbf{L_j}$ and $\mathbf{A_c}_{ij} = 0$ otherwise. For example, acquisitions take place on dates A, B, C, D which are equally spaced at time intervals of 1 year, and we form interferograms AB, BC, BD, AC. For a given pixel, the vector $\mathbf{b}$ contains the LOS displacement values in each interferogram. The matrix equation is then

$$\begin{pmatrix} -1 & +1 & 0 & 0 \\ 0 & -1 & +1 & 0 \\ 0 & -1 & 0 & +1 \\ -1 & 0 & +1 & 0 \end{pmatrix} \begin{pmatrix} c_A \\ c_B \\ c_C \\ c_D \end{pmatrix} = \begin{pmatrix} i_{AB} \\ i_{BC} \\ i_{BD} \\ i_{AC} \end{pmatrix} \tag{2}$$

[16] For any system, the number of unknowns is one greater than the rank of the design matrix. This is sometimes referred to as the 'fencepost' problem because there will always be one more post than fence panel in the same way there will always be one more acquisition than interferogram. As a result, the displacement must be solved relative to a reference acquisition (usually the first acquisition) at which point there is assumed to be zero displacement. This can be done either explicitly, by adding an additional constraint, $c_A = 0$, or implicitly, by removing an unknown (removing $\mathbf{A_{i1}}$

and x_{c1}). Since there are no errors on the simple example given, the explicit and implicit versions are equivalent. To illustrate the example, let $\mathbf{b} = [1, 1, 2, 2]$ mm. Using a standard least squares inversion technique gives values of $\mathbf{x_c} = [1, 2, 3]$ equivalent to a linear displacement rate of 1 mm/yr.

2.2. Incremental Displacement From InSAR

[17] In many cases, not all the interferograms can be linked into a single network forming unconnected subsets with at least one time step which is not directly constrained by data. This system is typically solved using a singular value decomposition subject to an L2 norm constraint which tends to minimize the cumulative displacement. *Berardino et al.* [2002] point out that this can produce physically unrealistic solutions in the event of data gaps or temporally overlapping SBAS subsets, and that this problem can be avoided by parameterizing the problem in terms of velocity. Because the deformation at Okmok is so nonlinear in time, we take the very similar approach of solving for incremental displacements in small time steps by expressing the equation for an individual interferogram by

$$\phi_{az} = \frac{4\pi}{\lambda}(d_{ab} + d_{bc} + d_{cd} + \ldots + d_{yz}) + \epsilon \tag{3}$$

[18] Using the notation from the previous example, we can define a new system of equations $\mathbf{A_d}x_d = b$. In this case, the model vector, x_d contains the incremental displacements in a series of time steps $[d_{AB}, d_{BC}, d_{CD}\ldots]$. Then, $\mathbf{A_{d}}_{ij} = 1$ for $\mathbf{H_{i1}} \leq \mathbf{L_j} < \mathbf{H_{i2}}$ and $\mathbf{A_{ij}} = 0$ otherwise. The matrix equation for our simple example is then

$$\begin{pmatrix} 1 & 0 & 0 \\ 0 & 1 & 0 \\ 0 & 1 & 1 \\ 1 & 1 & 0 \end{pmatrix} \begin{pmatrix} d_{AB} \\ d_{BC} \\ d_{CD} \end{pmatrix} = \begin{pmatrix} b_{AB} \\ b_{BC} \\ b_{BD} \\ b_{AC} \end{pmatrix} \tag{4}$$

[19] The model values represent the displacement in each time step and the cumulative displacement can be found by summing the values. By solving for the displacement in individual time periods rather than the cumulative displacement, we avoid the 'fencepost' problem. The matrix A will be rank L with L unknowns, so the system of equations requires no further smoothing constraints, or reference points. For our example values $\mathbf{b} = [1, 1, 2, 2]$ mm, we find $\mathbf{x_d} = [1, 1, 1]$ giving a cumulative displacements of $\mathbf{x_c} = [1, 2, 3]$, again equivalent to linear rate of 1 mm/yr.

2.3. GPS Observations

[20] GPS measurements record the absolute position of the instrument in three dimensions (easting, northing, height) and there are two ways we can address the GPS displacement vectors in ITRF to solve for the vector of incremental displacements, d. In this case, we will use the example of a single continuous GPS site and a single component, x, measured at regular time steps $t = 1, 2\ldots$. The first approach uses the displacement since the previous observation, and uses the identity as a design matrix, $\mathbf{Id} = \mathbf{x_t} - \mathbf{x_{t-1}}$

$$\begin{pmatrix} 1 & 0 & 0 \\ 0 & 1 & 0 \\ 0 & 0 & 1 \end{pmatrix} \begin{pmatrix} d_{x,12} \\ d_{x,23} \\ d_{x,34} \end{pmatrix} = \begin{pmatrix} x_2 - x_1 \\ x_3 - x_2 \\ x_4 - x_3 \end{pmatrix} \tag{5}$$

[21] The second method uses the cumulative displacement since the first observation, using a lower triangular matrix as a design matrix, $\mathbf{Ld} = \mathbf{x_t} - \mathbf{x_0}$

$$\begin{pmatrix} 1 & 0 & 0 \\ 1 & 1 & 0 \\ 1 & 1 & 1 \end{pmatrix} \begin{pmatrix} d_{x,12} \\ d_{x,23} \\ d_{x,34} \end{pmatrix} = \begin{pmatrix} x_2 - x_1 \\ x_3 - x_1 \\ x_4 - x_1 \end{pmatrix} \tag{6}$$

[22] Both approaches have advantages and disadvantages for noisy data. The first approach essentially differentiates the position measurements, and so is sensitive to uncorrelated noise between adjacent points. The second method deals with cumulative displacement, thus integrating the noise over the previous measurements and reducing the effect of random noise. However, since the first observation is used repeatedly, errors on that observation will percolate throughout the time series. By testing both methods, we find that for the data used here the second method provides a qualitatively cleaner result, so we use that.

[23] As previously described, *Berardino et al.* [2002] show that solving for velocity reduces the unphysical solutions which can occur when applying an L2 norm to displacements. This is effective for data sets with regular time steps, however, continuous GPS time series contains inevitable breaks which can be of the duration of a few days to several months (especially in the extreme climate of the Aleutians where physical access is seasonal). In this case, the velocity of the preceding time step is extrapolated across the data gap, amplifying small errors in individual time steps and causing step discontinuities in the time series. For this reason, we prefer to solve for incremental displacements with the result that in the absence of data for a given time step, we minimize the displacement over that step, regardless of its duration.

2.4. Single Step Inversion From Displacement Time Series to Volume Flux Rate

[24] The methods described in sections 2.1–2.3 calculate the temporal evolution of surface displacement in a single direction at a single location. In order to integrate the observations from spatially different locations and from different viewing geometries requires a model of the surface deformation. In the case of Okmok volcano, the source geometry has been shown to be fixed and simple. A point source model [*Mogi*, 1958] fits both InSAR and GPS observations [*Lu et al.*, 2010; *Fournier et al.*, 2009].

[25] The surface displacement, d at a given point, can be predicted using the scalar product of l and M where l is the three-component LOS unit vector obtained from incidence and heading angles for the InSAR observations and the unit direction vector for GPS (for example, east component = [0 1 0]). For the observation point at location $[x, y, z]$, M is the three-component displacement vector, $[m_x, m_y, m_z]$, predicted by the Mogi model with volume change ΔV and Poisson's ratio ν,

$$\begin{pmatrix} m_x \\ m_y \\ m_z \end{pmatrix} = \frac{\Delta V}{\pi}(1 - \nu) \begin{pmatrix} \frac{x}{R^3} \\ \frac{y}{R^3} \\ \frac{z}{R^3} \end{pmatrix} \tag{7}$$

where $R = (x^2 + y^2 + z^2)^{\frac{1}{2}}$ is the distance from source to observation. In this way, observations from several pixels,

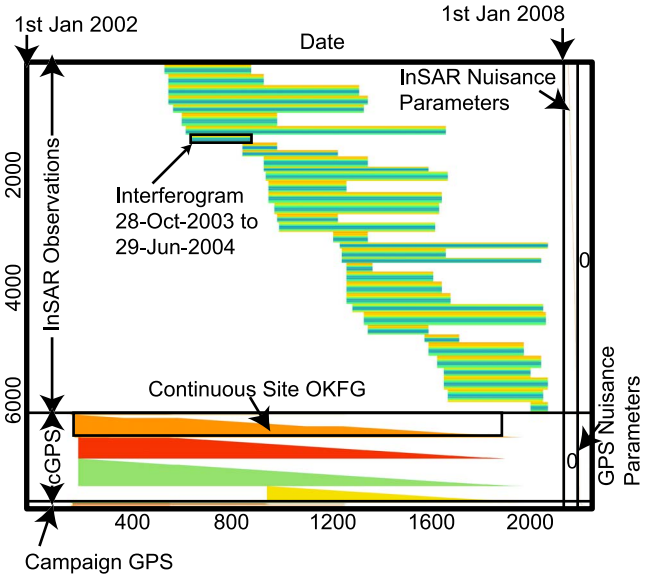

Figure 2. Structure of an example joint inversion design matrix covering the period 2002–2008. Columns represent parameters to be solved for (velocity on a given date, or nuisance parameter); rows represent observations (ordered InSAR; continuous GPS; campaign GPS). Colors represent the magnitude of the matrix values.

or GPS sites can be combined to estimate the incremental volume change of the Mogi source, v.

$$\begin{pmatrix} (\mathbf{l_a}.\mathbf{M_a})\mathbf{A_a} \\ (\mathbf{l_b}.\mathbf{M_b})\mathbf{A_b} \\ \vdots \end{pmatrix} \begin{pmatrix} v_{12} \\ v_{23} \\ v_{34} \\ \vdots \end{pmatrix} = \begin{pmatrix} \mathbf{b_a} \\ \mathbf{b_b} \\ \vdots \end{pmatrix} \tag{8}$$

where the subscripts a, b… represent the observation group. For example, if $\mathbf{d_a}$ contains all the observations for one component at a single GPS site, then $\mathbf{l_a}$ is the unit vector corresponding to the direction of that component, $\mathbf{M_a}$ is the three-component displacement vector caused by a volume change of 1 km^3 and A_a is the temporal design matrix described in sections 2.1–2.3. The structure of the design matrix is shown in Figure 2.

[26] The velocity solution can then be integrated up, taking into account the different durations of each time step, to give a final time series of volume change, as shown in Figure 4.

2.5. Nuisance Parameters and Weighting

[27] The methods described above assume that the only significant contribution to the observations is the surface displacement caused by Mogi source volume changes. Two types of noise exist: those for which the temporal or spatial characteristics are well known (e.g., offset due to reference frame changes) and those with random characteristics (e.g., atmospheric water vapor).

[28] The first of these can be included in the inversion and a simultaneous solution found for both the model and "nuisance parameters" (Figure 2), and the second can be dealt with by weighting the inversion using appropriate error estimates.

[29] In the joint inversion, we solve for three types of nuisance parameters: (1) phase offsets in the interferograms caused by the choice of reference pixel; (2) a constant offset for each component at each GPS site caused by noise on the first observation; and (3) a constant velocity in each GPS component caused by translation of the network relative to ITRF.

[30] There are several other sources of noise which it is not possible to solve for directly, hence we estimate the relative errors on each observation and weight the inversion [*Menke*, 1989]. We use a diagonal variance-covariance matrix, $\mathbf{\Sigma}$, which for three points with errors σ_a, σ_b, σ_c is given by

$$\mathbf{\Sigma} = \begin{pmatrix} \sigma_a^2 & 0 & 0 \\ 0 & \sigma_b^2 & 0 \\ 0 & 0 & \sigma_c^2 \end{pmatrix} \tag{9}$$

and for an inversion of the form $\mathbf{Ax} = \mathbf{b}$, the solution $\mathbf{x}$ and associated error $\mathbf{\Sigma_x}$ are given by

$$\mathbf{x} = \left[\mathbf{A}^T\mathbf{\Sigma}^{-1}\mathbf{A}\right]^{-1}\mathbf{A}^T\mathbf{\Sigma}^{-1}\mathbf{b} \tag{10}$$

$$\mathbf{\Sigma_x} = \left[\mathbf{A}^T\mathbf{\Sigma}^{-1}\mathbf{A}\right]^{-1} \tag{11}$$

[31] The typical error on each interferogram is estimated by calculating the standard deviation of the far-field values (beyond a certain radius from the source location). The daily GPS uncertainties are estimated during processing with the GIPSY-OASIS software package [*Zumberge et al.*, 1997] and includes uncertainty from satellite clock, orbit location, atmospheric path effects and other unmodeled factors. In the weekly data, the uncertainties are based on the combined weekly average position and combined daily uncertainties.

[32] This approach assumes each observation is independent, but there are spatial and temporal correlations in both data sets. In the InSAR, spatial correlation between pixels in an interferogram is caused by the smooth nature of atmospheric water vapor fields [e.g., *Hanssen*, 2001] and temporal correlations between interferograms are caused by repeated use of master or slave images. Correlations between the GPS components at a single site are a natural result of the transformation between the distance to satellites and the position of an antenna on the ground. In this case, the deformation signal is large and the temporal correlation between GPS observations is relatively small.

[33] It is possible to construct complete variance-covariance matrices to include each of these terms [e.g., *Biggs et al.*, 2007, 2009; *Wang et al.*, 2009]. However, by ignoring the off-diagonal terms (the covariances), we reduce the variance-covariance matrix to a diagonal matrix, removing the need for computationally expensive inversions.

2.6. Computational Restrictions and Downsampling

[34] The design matrix in this problem is of dimensions $[M \times N]$, where M is the number of observations and N is the number of time steps. Sixteen years of 1 day time steps would give $N \sim 6000$. The number of GPS observations is dominated by the continuous data for which we have 4 years of daily three-component observations at 4 continuous GPS sites ($4 \times 4 \times 3 \times 365 \sim 20{,}000$). We use 95 interferograms,

Table 2. Source Locations for Okmok Magma Chamber From Previous Studies and the Range of Inversion Carried Out in This Study[a]

Inversion	UTM East (km)	UTM North (km)	Depth (m)
InSAR [*Lu et al.*, 2005]	690.5	5923.6	3.1
GPS [*Fournier et al.*, 2009]	690.0	5924.3	3.0
Joint (this study)	690.3	5923.6	3.4
InSAR (this study)	690.7	5923.6	3.4
GPS (this study)	690.3	5923.6	3.4

[a]Depths are below the surface at ~360 m.

each of which has 1 million pixels making a total M = 95,000,000. The computation is memory-intensive and it is necessary to reduce the size of the problem by downsampling the data and to use algorithms and data formats specifically designed to deal with large problems.

[35] The number of InSAR observations depends on the downsampling of the interferograms; we use a grid of points with a sample spacing of 800 m within 6 km of the source, and 4 km outside this radius we end up with ~14000 measurements. We reduce the GPS to weekly observations which produces ~2700 measurements. Thus, by downsampling the data and making use of sparse storage facilities the inversion can be quickly (< 1 min) and efficiently carried out on a current lab-type processing computer.

3. Results of Joint Inversion

3.1. Source Location

[36] Both InSAR [*Lu et al.*, 2005, 2010] and GPS [*Fournier et al.*, 2009] studies have shown that the source of inflation and deflation can be represented by a fixed location point source, to within error. However, the precise location differs slightly between studies, with the source inferred from the InSAR located 840 m SSE of that inferred from GPS (Table 2). Both studies use a point source, but the model of *Fournier et al.* [2009] includes a correction for topography. Other possible causes of the discrepancy are (1) the source is not stable and the differences in temporal sampling introduce a bias, (2) the source is not a point source in an elastic halfspace and differences in spatial sampling introduce a bias, (3) different inversion techniques introduce bias, and (4) the differences in source location are within error of either system; that is, the local minimums are numerical artefacts and a solution exists which does not significantly degrade the fit to either data set. Given the findings of *Lu et al.* [2005, 2010] and *Fournier et al.* [2009], we conclude that the assumption of a simple, stable source is valid and use the joint inversion to investigate possibilities 3 and 4.

[37] We calculate the weighted residual for the inversion and carry out a three-dimensional grid search (latitude, longitude, depth) to find the minimum for a GPS-only, InSAR-only and joint inversion (Figure 3). The grid spacing is 200 m in horizontal and 400 m in depth. To improve the speed of computation, we discard the continuous GPS sites, using only the campaign sites which offer better spatial coverage and use InSAR observations from the Envisat era (2002–2008) only. The GPS-only misfits show a clear minimum close to the location of *Lu et al.* [2010] at a depth of 3.4 km. The InSAR-only grid search finds a broader minimum at the same depth (3.4 km), located 400 m to the east. The minimum RMS of 8.2 mm is consistent with the magnitude of noise expected from tropospheric water vapor delays. The joint inversion grid search finds a steeper minimum than from either individual data set at the same location as the GPS-only inversion. The best fitting source location is very close (within 200 m) to that found by *Lu et al.* [2010].

[38] The differences between the InSAR-only location and the InSAR study of *Lu et al.* [2005] and the GPS-only location and the GPS study of *Fournier et al.* [2009] suggest that inversion method (which includes data selection and data resampling) play a significant role in the discrepancy between source locations. In particular, the GPS study of *Fournier et al.* [2009] used both campaign and continuous GPS data and the inclusion of the numerous cGPS data points tends to weight the source location to fit the near field deformation. However, even when using the same inversion strategy, the GPS-only source location is 400 m west of the InSAR-only location. Although the best fitting joint location does not provide the lowest numerical misfit to the interferograms, inspection of the models and residuals does not show a noticeable degradation of the fit, suggesting that the difference is not significant. We conclude that formal error analysis, which only includes errors in the observations underestimate the true errors on the source location, which

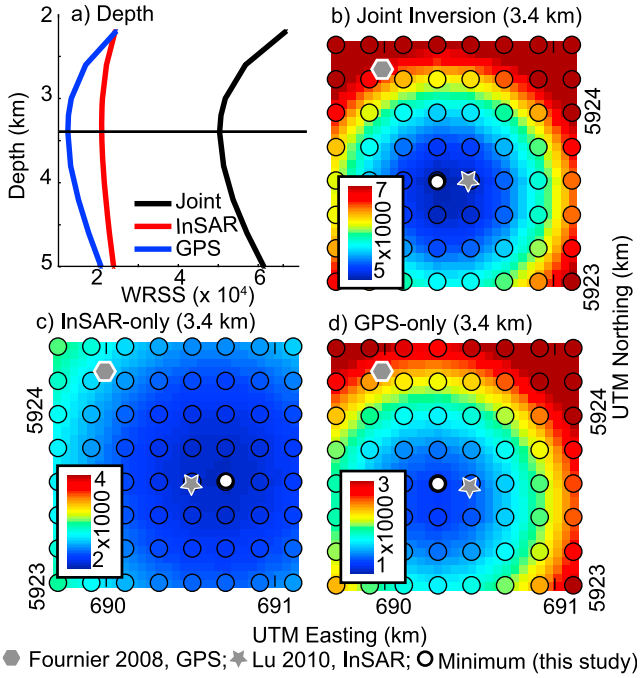

Figure 3. Grid search to find best fitting source location. A weighted misfit is calculated for each inversion and plotted. (a) Misfit against depth; for each depth slice, a grid search is performed to find the best horizontal location. (b) joint inversion misfits showing a smooth, localized minimum. (c) InSAR-only. (d) GPS-only. Hexagons are from *Fournier* [2008], stars are from *Lu et al.* [2010], and circles are from this study.

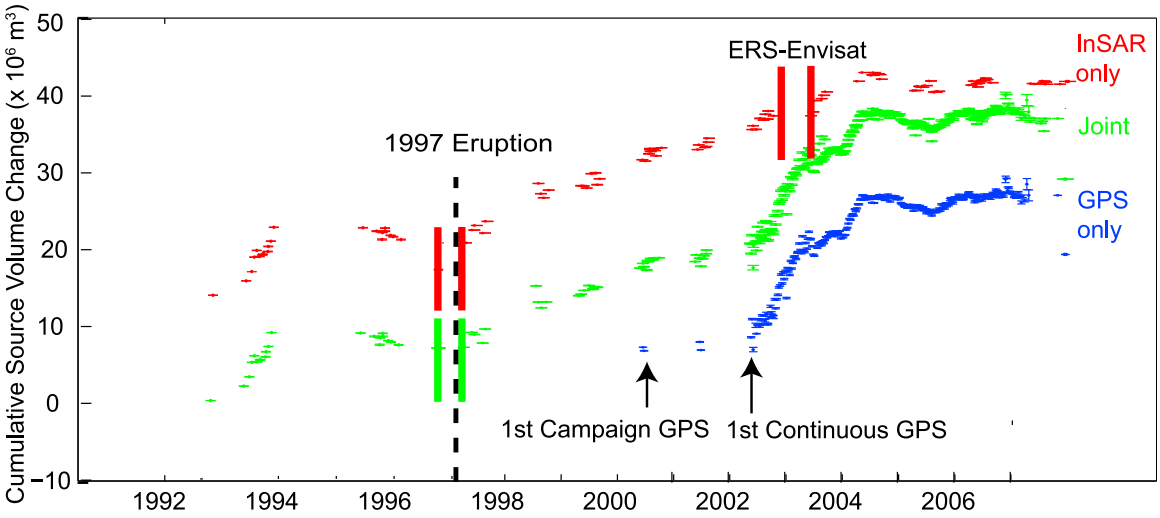

Figure 4. Source volume estimates from joint (green), InSAR-only (red), and GPS-only (blue) inversions of geodetic data from Okmok Volcano, 1992–2008. All three records show the same patterns of inflation and deflation and are offset due to differences in the start time and volume. The joint inversion time series matches the shape of the individual inversion, taking advantage of both the high temporal resolution of the GPS data and the 15 year duration of the InSAR data. There are two discontinuities in the InSAR time series: the 1997 eruption and the data gap between ERS and Envisat satellites. There is one discontinuity in the joint time series at the time of the 1997 eruption. Campaign GPS data started in 2000, and continuous GPS sites began in 2002.

also include biases introduced by the inversion technique and erroneous assumptions.

3.2. Comparison to Individual Inversions

[39] Using the best fitting location described in section 3.1, we investigate the differences in time series between the InSAR-only, GPS-only and joint time series and their fits to the data (Figure 4). The results from all three inversions show the same general pattern of inflation and deflation as previous studies. Although ignoring topographic effects can overestimate volume estimates by as much as 8% in the case of Etna [*Cayol and Cornet*, 1998], the topography here is not extreme and the volume estimates (2.18×10^7 m^3) only slightly greater that of *Fournier et al.* [2009] ($2.1 \pm 0.05 \times 10^7$ m^3) especially when the errors are taken into account. The offset between records is caused by the differences in start time and volume: the InSAR-only and GPS-only data sets start with zero volume in 1992 and 2000, respectively. The joint and InSAR-only time series have been plotted separated by 10×10^6 m^3 for ease of viewing.

[40] The InSAR-only inversion only has time steps during the summer months since interferograms made using acquisitions during the snow-covered winter months are usually incoherent [*Lu et al.*, 2005; *Biggs et al.*, 2007]. The year-to-year inflation and deflation signals are well resolved and closely match those recorded from the GPS data set where available. However, the ~4–5 satellite acquisitions per summer are not sufficient to resolve the smaller volume changes within an individual summer with any degree of confidence.

[41] The GPS time series starts in 2001 and for the first 2 years campaign measurements were made during the summer months only [*Miyagi et al.*, 2004] giving year-to-year volume changes only. Following the installation of continuous sites in 2003, the measurements become more frequent, and in this inversion we use weekly data, although daily measurements are available. The magnitude and shape of the volume change time series closely matches that found by *Fournier et al.* [2009] from the same data set. The nuisance parameters which reflect the error on the first GPS observation for each component at each station are 0.1 ± 5 mm. The translation of the network relative to the reference frame is estimated to be [−9.7, −22.2, +4.8] mm/yr. There is a significant difference in the eastward component between this and the North America reference frame [-3.3 ± 0.1, -21.5 ± 0.2, 2.3 ± 0.3] estimated by *Sella et al.* [2007]. However, it is comparable to the previous estimate of [-8.3 ± 0.2, -21.8 ± 0.2, $+2.3 \pm 0.3$] mm/yr from *Fournier et al.* [2009], who attribute the differences to a combination of Bering Plate rotation [*Cross and Freymueller*, 2008] and interseismic strain from the subduction zone.

[42] The joint inversion combines the 16 year record of InSAR data with the shorter but denser continuous GPS observations, thus fulfilling its design criteria. The cumulative volume change is consistent with those from the inversions of the individual data sets but benefits from the temporal characteristics of both data sets.

3.3. Data Gaps

[43] There are two periods that are not covered by the InSAR data: the 1997 eruption and the transition between the satellites ERS and Envisat. Although an interferogram exists spanning the 1997 eruption [*Lu et al.*, 2005], the subsampling algorithm applied to the other interferograms is not appropriate for the much higher coeruptive displacement gradients. Although the inversion algorithm is flexible enough to include different numbers of observations for each interferogram, and it would be possible to use different subsampling algorithm for intereruptive and coeruptive interferograms, for simplicity and consistency, we prefer to

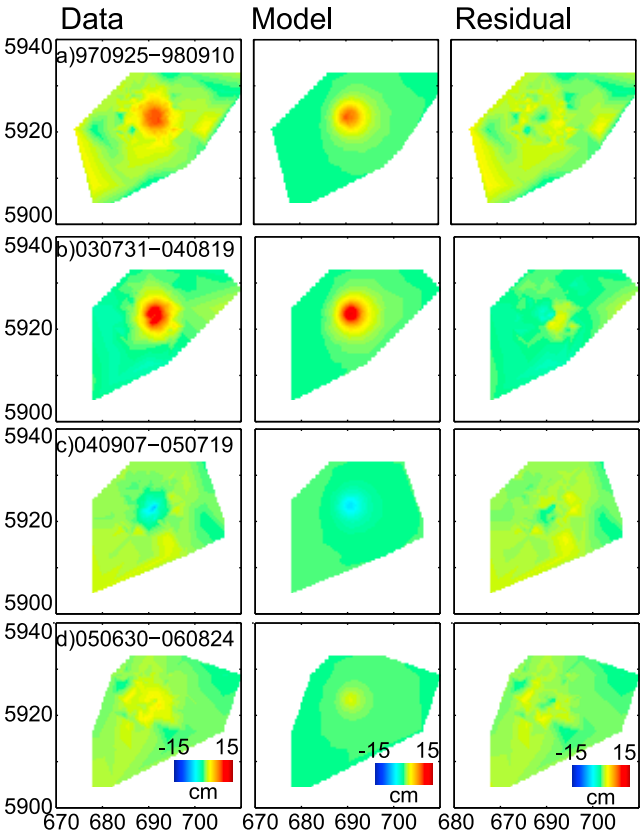

Figure 5. InSAR residuals. Example interferograms showing (left) observations, (middle) model, and (right) residuals. The interferograms are chosen to represent periods of interest: (a) 25 September 1997 to 10 September 1998, period of reinflation following the 1997 eruption; (b) 31 July 2003 to 19 August 2004, the rapid pulse of inflation between eruptions; (c) 7 September 2004 to 19 July 2005, subsidence following the pulse of rapid inflation; and (d) 30 June 2005 to 24 August 2006, period of little or no motion during 2005–2008. In each case, the model fits the data well, and the residuals show features consistent with atmospheric signals. The postemplacement subsidence of the 1958 and 1977 lava flows is visible in some longer time span interferograms [*Lu et al.*, 2005].

apply the same subsampling algorithm to all interferograms. Furthermore, the volume change of the coeruptive time step is an order of magnitude larger than that of the intereruptive time steps. This violates the implicit assumption used in solving rank-deficit systems of equations which minimize the L2 norm, hence finding the smallest absolute values consistent with the observations [*Berardino et al.*, 2002].

[44] The second data gap is between the failure of the ERS-2 gyroscopes in June 2001 and the beginning of the Envisat data set in 2003. During this period, we were fortunate to obtain ERS-2 images in whose Doppler centroids are adequate for interferogram generation. Although both satellites operate at C band, small differences in the wavelength mean that ERS-Envisat cross interferometry, while possible, is only practical in areas of low topography. The ERS-Envisat data gap does not affect the joint inversion since the same time period is covered by the GPS data.

[45] For periods where no data is available, the solution provided by standard inversion algorithms assumes that the volume change is zero (Figure 4). It is simple to identify these gaps in the data from the structure of the design matrix. For eruptions, we split the time series at this point, thus reducing the computational size of the problem. When reconstructing the cumulative time series, we use external data to rejoin the sections of time series (Figure 7). For the 1997 eruption, we use the best fitting eruption volume of $-47 \pm 2 \times 10^6$ m^3 found from modeling the coeruptive interferogram [*Lu et al.*, 2005].

3.4. Residuals

[46] In order to verify that the final time series matches the individual observations, we inspect four sample interferograms chosen to represent different periods of behavior. Figure 5a illustrates the period of reinflation following the

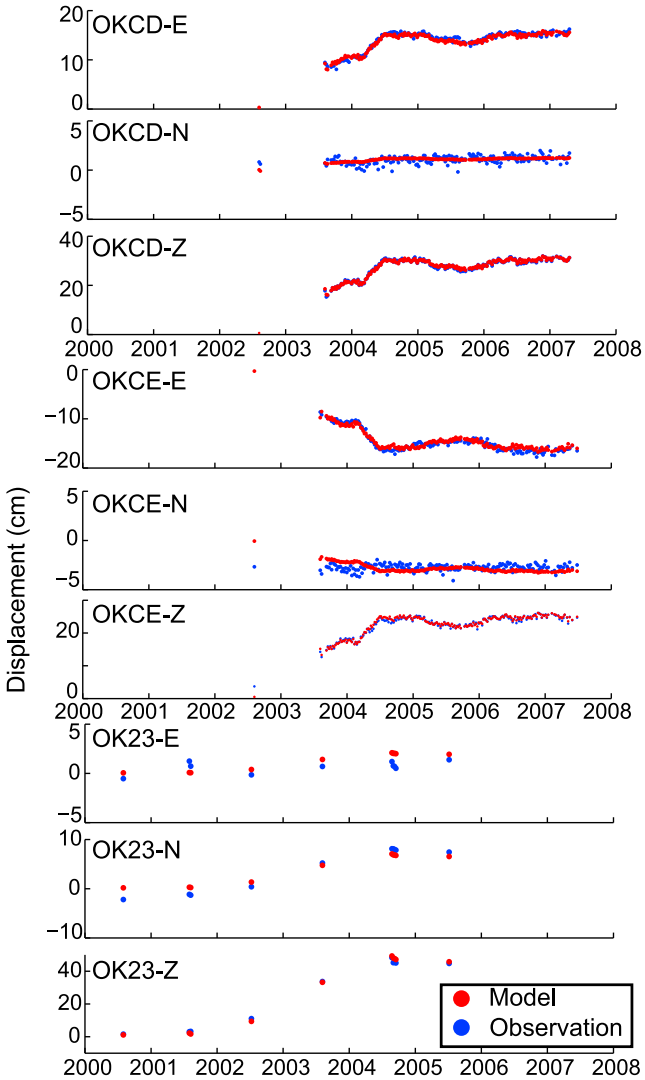

Figure 6. GPS residuals. Example time series at selected sites. OKCD and OKCE have been continuous GPS sites since 2002. OK23 is had annual campaign measurements from 2000 to 2005. The models are shown in red, and observations are shown in blue. Note the differences in scale between plots.

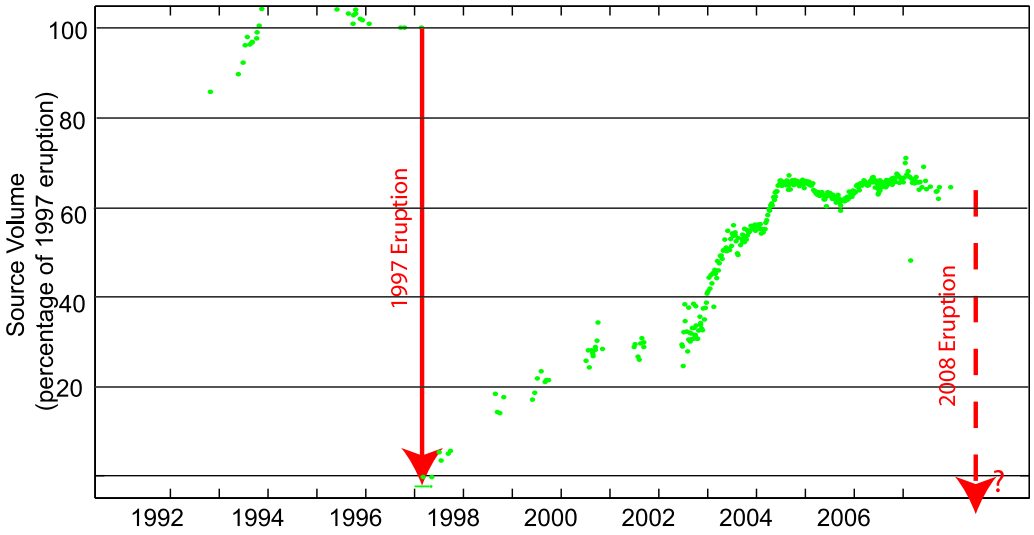

Figure 7. Cycles of discharge and recharge for the magma chamber at Okmok Volcano calculated from a joint inversion of InSAR, continuous and campaign GPS.

1997 eruption. Figure 5b illustrates the rapid inflation between eruptions. Figure 5c illustrates the subsidence following the pulse of rapid inflation. Figure 5d illustrates a period of little or no motion. In each case, the model fits the sign and amplitude of the data well, showing that the changes in deformation pattern in the final time series are required by the InSAR as well as the GPS data, and cannot be a numerical artefact. In most cases, the residuals are consistent with the magnitude and pattern of atmospheric artefacts observed in nondeforming regions. In some longer term interferograms, the postemplacement subsidence of the lava flows can be seen [*Lu et al.*, 2005].

[47] Similarly, we check the fit to the GPS data using selected test sites (Figure 6). The continuous site OKCD is located due east and OKCE due west of the source. Both show positive vertical displacements (uplift); negligible north-south displacements and opposite east-west displacements: the site to the east moves east, the site to the west moves west. The campaign site OK23 is due north of the source and has annual measurements for 6 years. In all cases, the model data fits the sign and magnitude well, matching both short-term variations and long-term trends for both campaign and continuous data. The small mismatch that remains is likely to be the result of an oversimplified source model. Future refinements will involve multiple sources and more complex source geometries.

4. Discussion

4.1. Volume Changes

[48] The volume changes shown in Figure 7 follow the same pattern as previously reported from studies of the separate data subsets [*Lu et al.*, 2005; *Fournier et al.*, 2009]. In general, the source has been dominantly inflating during intereruptive periods (pre-1997 and 1998–2008) and deflating during eruptions. However, significant variations exist in the rate of inflation and there have been several periods of minor deflation. From 1992 to 1995 there was inflation followed by a small amount of deflation from 1995 to 1996 preceding the 1997 eruption. Following the eruption, gradual inflation resumed from 1997 to 2002. There are two pulses of rapid inflation: summer 2002 to late 2003, and spring-summer 2004. The second of these pulses of rapid inflation is clearly followed by a small amount of deflation. Both InSAR and GPS show a period of rapid inflation in the few months immediately preceding the 2008 eruption which is outside the time span of the results presented here [*Lu et al.*, 2010].

[49] Conceptual models of magma systems assume either that a pulse of magma influx causes rapid inflation such that the overpressure exceeds some critical threshold, causing an eruption, or that continuous magma pressure from a deeper source which causes rapid reinflation of the magma source immediately following an eruption. At Okmok, the majority of the inflation occurred in the middle of the intereruptive period, neither triggering nor triggered by eruptive activity. The slowing of inflation pre-2008 and deflation pre-1997 are likely indicators that the chamber was close to maximum capacity and critical pressure. The magma chamber appears to have remained in this relatively stable state for a period of years with only a small additional inflation over a short time occurring before the eruption. It seems likely that external factors or small, random perturbations within the system caused a rapid, runaway effect on the time scale of a few months.

4.2. Application to Volcano Monitoring

[50] The quantity of geodetic information available is growing rapidly: more volcanoes are being instrumented with dense GPS networks and more SAR satellites are launched. The next stage is to use this geodetic information for real-time practical rather than retrospective research purposes. From a decision-making perspective, an integrated estimate of magma volume flux and location is easier to interpret than a set of displacement measurements produced using measurements techniques with different temporal and spatial sensitivities. The work presented here is one example of a joint inversion algorithm by which this could be achieved. Furthermore, the adaptability of the algorithm to observations

with different spatial and temporal characteristics mean it would be simple to adapt to include real-time data.

[51] Both InSAR and GPS suffer data availability issues from a monitoring perspective. GPS measurements require ground-based equipment that can be damaged by volcanic activity or difficult to access in times of high alert. Satellite observations, while remote, are less frequent and can suffer unpredictable data gaps due to poor baselines or low coherence often causing a significant time lag. By combining the data sets rather than relying on a single technique, the chances of producing useful measurements at the critical time are increased.

[52] While planning for future satellite missions, the optimum repeat time of SAR satellites for deformation studies is frequently debated [*Fournier et al.*, 2010]. The comparison between data sets in this study clearly shows the advantage of weekly GPS measurements over the InSAR observations which essentially have a 1 year repeat in this region. However, major limitation on the density of the InSAR time series is the lack of coherent observations in the winter months rather than the 35 day repeat cycle of the ERS and Envisat satellites. During the period 2003–2008, Envisat collected images of Okmok using several different beam modes, and by combining these to estimate the volume flux rather than directly calculating surface displacement, we produce a time series with a minimum spacing of 8 days, equivalent to the sampling favored by the continuous GPS study [*Fournier et al.*, 2009]. This is comparable to the repeat times proposed for future satellites including ESA's Sentinel Missions (6–12 days) and NASA's DesDynI (8 days). Even so, there are likely to be variations on much shorter periods (subdaily) which will only be picked up on continuously monitoring instruments [*Mattia et al.*, 2008].

5. Conclusions

[53] This paper explains a method for combining InSAR, continuous GPS and campaign GPS data for determining the time-varying change in volume for a magmatic source using a modified version of SBAS [*Berardino et al.*, 2002] The method is tested on real data from Okmok volcano where a 16 year time series is produced spanning the 1997 eruption. The results are shown to match the original data and are compatible with previously published results from individual data sets [e.g., *Fournier et al.*, 2009; *Lu et al.*, 2010]. This algorithm has applications for use in volcano monitoring where individual data streams may not be available at crucial times and an integrated estimate of magma volume flux and location is easier to interpret than a set of displacement measurements produced using different techniques.

[54] **Acknowledgments.** J.B. was supported by a Rosenstiel Postdoctoral Fellowship from the University of Miami and a Lindemann Fellowship from the English Speaking Union and would like to thank staff at the Cascades Volcano Observatory for a pleasant and informative visit. GPS surveys at Okmok were supported by the Alaska Volcano Observatory (a joint venture of the University of Alaska, U.S. Geological Survey, and Alaska Division of Geological and Geophysical Surveys) as part of the Volcano Hazards Program, with additional funds by the State of Alaska and by the Federal Aviation Administration. Z.L. was supported by NASA's Earth Surface and Interiors grant 2005-0021 and USGS Volcano Hazards Program. J.F. was supported by the Alaska Volcano Observatory, under funding by USGS. We thank two anonymous reviewers for their constructive reviews.

References

Berardino, P., G. Fornaro, R. Lanari, and E. Sansosti (2002), A new algorithm for surface deformation monitoring based on small baseline differential SAR interferograms, *IEEE Trans. Geosci. Remote Sens.*, *40*, 2375–2383, doi:10.1109/TGRS.2002.803792.

Biggs, J., T. Wright, Z. Lu, and B. Parsons (2007), Multi-interferogram method for measuring interseismic deformation: Denali Fault Alaska, *Geophys. J. Int.*, *170*, 1165–1179, doi:10.1111/j.1365-246X.2007.03415.x.

Biggs, J., R. Burgman, J. Freymueller, Z. Lu, B. Parsons, I. Ryder, G. Schmalzle, and T. Wright (2009), The postseismic response to the 2002 M7.9 Denali Fault earthquake: Constraints from InSAR 2003–2005, *Geophys. J. Int.*, *176*, 353–367, doi:10.1111/j.1365-246X.2008.03932.x.

Bürgmann, R., P. A. Rosen, and E. J. Fielding (2000), Synthetic aperture radar interferometry to measure Earth's surface topography and its deformation, *Annu. Rev. Earth Planet. Sci.*, *28*, 169–209, doi:10.1146/annurev.earth.28.1.169.

Cayol, V., and F. H. Cornet (1998), Effects of topography on the interpretation of the deformation field of prominent volcanoes—Application to Etna, *Geophys. Res. Lett.*, *25*, 1979–1982, doi:10.1029/98GL51512.

Cervelli, P., P. Segall, F. Amelung, H. Garbeil, C. Meertens, S. Owen, A. Miklius, and M. Lisowski (2002), The 12 September 1999 Upper East Rift Zone dike intrusion at Kilauea Volcano, Hawaii, *J. Geophys. Res.*, *107*(B7), 2150, doi:10.1029/2001JB000602.

Cross, R. S., and J. T. Freymueller (2008), Evidence for and implications of a Bering plate based on geodetic measurements from the Aleutians and western Alaska, *J. Geophys. Res.*, *113*, B07405, doi:10.1029/2007JB005136.

Ferretti, A., C. Prati, and F. Rocca (2001), Permanent scatterers in SAR interferometry, *IEEE Trans. Geosci. Remote Sens.*, *39*, 8–20.

Fialko, Y., Y. Khazan, and M. Simons (2001a), Deformation due to a pressurized horizontal circular crack in an elastic half-space, with applications to volcano geodesy, *Geophys. J. Int.*, *146*, 181–190, doi:10.1046/j.1365-246X.2001.00452.x.

Fialko, Y., M. Simons, and D. Agnew (2001b), The complete (3-D) surface displacement field in the epicentral area of the 1999 M_w7.1 Hector Mine earthquake, California, from space geodetic observations, *Geophys. Res. Lett.*, *28*, 3063–3066, doi:10.1029/2001GL013174.

Finney, B., S. Turner, C. Hawkesworth, J. Larsen, C. Nye, R. George, I. Bindeman, and J. Eichelberger (2008), Magmatic differentiation at an island-arc caldera: Okmok Volcano, Aleutian Islands, Alaska, *J. Petrol.*, *49*(5), 857–884, doi:10.1093/petrology/egn008.

Fournier, T., J. Freymueller, and P. Cervelli (2009), Tracking magma volume recovery at Okmok Volcano using GPS and an unscented Kalman filter, *J. Geophys. Res.*, *114*, B02405, doi:10.1029/2008JB005837.

Fournier, T. J., M. Pritchard, and S. Riddick (2010), Duration, magnitude, and frequency of subaerial volcano deformation events: New results from Latin America using InSAR and a global synthesis, *Geochem. Geophys. Geosyst.*, *11*, Q01003, doi:10.1029/2009GC002558.

Gudmundsson, S., F. Sigmundsson, and J. M. Carstensen (2002), Three-dimensional surface motion maps estimated from combined interferometric synthetic aperture radar and GPS data, *J. Geophys. Res.*, *107*(B10), 2250, doi:10.1029/2001JB000283.

Hanssen, R. F. (2001), *Radar Interferometry: Data Interpretation and Analysis*, Kluwer Acad., Norwell, Mass.

Larsen, J., et al. (2009), Eruption of Alaska volcano breaks historic pattern, *Eos Trans. AGU*, *90*, 173–174, doi:10.1029/2009EO200001.

Lu, Z., D. Mann, and J. Freymueller (1998), Satellite radar interferometry measures deformation at Okmok Volcano, *Eos Trans. AGU*, *79*, 461, doi:10.1029/98EO00348.

Lu, Z., D. Mann, J. T. Freymueller, and D. J. Meyer (2000), Synthetic aperture radar interferometry of Okmok Vvolcano, Alaska: Radar observations, *J. Geophys. Res.*, *105*, 10,791–10,806, doi:10.1029/2000JB900034.

Lu, Z., E. Fielding, M. R. Patrick, and C. M. Trautwein (2003), Estimating lava volume by precision combination of multiple baseline spaceborne and airborne interferometric synthetic aperture radar: the 1997 eruption of Okmok Volcano, Alaska, *IEEE Trans. Geosci. Remote Sens.*, *41*, 1428–1436, doi:10.1109/TGRS.2003.811553.

Lu, Z., T. Masterlark, and D. Dzurisin (2005), Interferometric synthetic aperture radar study of Okmok Volcano, Alaska, 1992–2003: Magma supply dynamics and postemplacement lava flow deformation, *J. Geophys. Res.*, *110*, B02403, doi:10.1029/2004JB003148.

Lu, Z., D. Dzurisin, J. Biggs, C. Wicks Jr., and S. McNutt (2010), Ground surface deformation patterns, magma supply, and magma storage at Okmok Volcano, Alaska, from InSAR analysis: 1. Intereruption deformation, 1997–2008, *J. Geophys. Res.*, *115*, B00B02, doi:10.1029/2009JB006969.

Mann, D., J. Freymueller, and Z. Lu (2002), Deformation associated with the 1997 eruption of Okmok Volcano, Alaska, *J. Geophys. Res.*, *107*(B4), 2072, doi:10.1029/2001JB000163.

Masterlark, T. (2007), Magma intrusion and deformation predictions: Sensitivities to the Mogi assumptions, *J. Geophys. Res.*, *112*, B06419, doi:10.1029/2006JB004860.

Mattia, M., M. Palano, M. Aloisi, V. Bruno, and Y. Bock (2008), High rate GPS data on active volcanoes: An application to the 2005–2006 Mt. Augustine (Alaska, USA) eruption, *Terra Nova*, *20*, 134–140, doi:10.1111/j.1365-3121.2008.00798.x.

Menke, W. (1989), *Geophysical Data Analysis: Discrete Inverse Theory*, Academic, San Diego, Calif.

Miller, T. P., R. G. McGimsey, J. R. Richter, J. R. Riehle, C. J. Nye, M. E. Yount, and J. A. Dumoulin (1998), Catalog of the historically active volcanoes of Alaska, *U.S. Geol. Surv. Open File Rep., 98-582*, 104 pp.

Miyagi, Y., J. T. Freymueller, F. Kimata, T. Sato, and D. Mann (2004), Surface deformation caused by shallow magmatic activity at Okmok Volcano, Alaska, detected by GPS campaigns 2000–2002, *Earth Planets Space*, *56*, e29–e32.

Mogi, K. (1958), Relations between eruptions of various volcanoes and the deformations of the ground surfaces around them, *Bull. Earthquake Res. Inst. Univ. Tokyo*, *36*, 99–134.

Okada, Y. (1985), Surface deformation due to shear and tensile faults in a half-space, *Bull. Seismol. Soc. Am.*, *75*, 1135–1154.

Samsonov, S., and K. Tiampo (2006), Analytical optimization of a dinsar and gps dataset for derivation of three-dimensional surface motion, *Geosci. Remote Sens. Lett.*, *3*(1), 107–111, doi:10.1109/LGRS.2005.858483.

Sella, G. F., S. Stein, T. H. Dixon, M. Craymer, T. S. James, S. Mazzotti, and R. K. Dokka (2007), Observation of glacial isostatic adjustment in "stable" North America with GPS, *Geophys. Res. Lett.*, *34*, L02306, doi:10.1029/2006GL027081.

Wang, H., T. J. Wright, and J. Biggs (2009), Interseismic slip rate of the northwestern Xianshuihe fault from InSAR data, *Geophys. Res. Lett.*, *36*, L03302, doi:10.1029/2008GL036560.

Wright, T., B. Parsons, and Z. Lu (2004), Toward mapping surface deformation in three dimensions using InSAR, *Geophys. Res. Lett.*, *31*, L01607, doi:10.1029/2003GL018827.

J. Biggs, NCEO, Department of Earth Sciences, University of Oxford, South Parks Road, Oxford OX1 3AN, UK. (juliet.biggs@earth.ox.ac.uk)

T. Fournier, Department of Earth Science, Rice University, PO Box 1892, Houston, TX 77251, USA.

J. T. Freymueller, Geophysical Institute, University of Alaska Fairbanks, 903 Koyukuk Dr., PO Box 757320, Fairbanks, AK 99775-7320, USA.

Z. Lu, USGS Cascades Volcano Observatory, 1300 SE Cardinal Ct., Bldg. 10, Ste. 100, Vancouver, WA 98683-9589, USA.